Multiphysics transport modeling in karst aquifers using the Euler-Lagrange approach and Control Volume Isogeometric analysis (CV-IGA): Laboratory verification in 3-D physical models

Marin Zelenika[1], Hrvoje Gotovac[1,*]

[1]Faculty of Civil Engineering, Architecture and Geodesy, University of Split, Matice hrvatske 15, 21000 Split.

E-mails: marin.zela@gmail.com, hrvoje.gotovac@gradst.hr

*Corresponding Author

Submitted to Advances in Water Resources

Abstract:

Karst flow and transport modeling is faced with many difficulties, mainly due to complex karst heterogeneity multiscale structure and inability to measure all sufficient input and output data. Among others, special problem is verification of karst flow and transport models under realistic catchment conditions. Therefore, we have recently built large 3-D physical models to develop and verify reliable flow and transport karst methodology under strongly controlled laboratory conditions. Salt tracer tests have been performed under different flow and injection conditions including the different conduits with free and pressurized flow, with and without precipitation as well as borehole and surface tracer injection. Results show that complex distributed karst flow and transport model is needed, based on Control Volume Isogeometric Analysis (CV-IGA), Eulerian-Langrage treatment of advection and dispersion and simple advection exchange term, to successfully reproduce salt tracer tests with good accuracy.

Key words: karst flow and transport modelling, 3-D physical models, Control Volume Isogeometric Analysis (CV-IGA), salt tracer tests

1. Introduction

Karst aquifers provide vulnerable water resources accounting for 25 % of the world groundwater resources. Croatian karst aquifers are located in many coastal aquifers and well known as highly karstified aquifers presenting very valuable and sensitive water resources. For example, Jadro spring ensures water resources for around 300 000 people in Split region, but any contamination inside the catchment can cause pollution of spring in a very short time, especially in comparison with other type of aquifers. Karst aquifers have complex characteristics that make them different from other aquifers (Bakalowicz 2005). They form in soluble rocks such as dolomite and limestone, and the dissolution process creates complex networks of preferential flow pathways that are difficult to locate. A karst aquifer is typically characterized by sinkholes, caves, springs, conduits and underground drainage systems formed by dissolution, internal drainage, and collapse processes. Karst aquifer permeability consists of: Matrix (or inter-granular) permeability of the bedrock itself, Fracture permeability and Conduit permeability. The flow fields through each of these permeability types operate on different scales (Teutsch and Sauter, 1991).

Because of the high heterogeneity and anisotropy of hydraulic parameters in a karst system, determination of their distribution over the system always deals with approximations in conceptual and numerical models. The effect of such approximations must be addressed as uncertainties in the results (e.g., Kovacs and Sauter 2007). There are two general modeling approaches in karst systems, (1) spatially lumped and (2) spatially distributed models.

Spatially lumped models (sometimes also called global models or “black box” models) simulate the global hydraulic, physical or chemical response of the aquifer output at a spring (e.g., spring discharge, concentrations in spring water) to the input into the aquifer system in the spring catchment (e.g., groundwater recharge, infiltrating rainfall and solutes) (Sauter et al. 2006). Spatial variations of flow patterns in the aquifer are not considered. Lumped-parameter models involve a mathematical analysis of temporal variations in spring discharge (hydrograph) or in

spring chemical concentration (chemograph) to give an understanding of the overall water balance in the karst system or an interpretation of groundwater quality, and fundamental information on the hydraulic behavior of the entire system. Lumped-parameter models are, however, limited in their ability to provide direct information about karst aquifer hydraulic and transport parameters, flow directions, and velocity.

Distributed models discretize the model domain, try to relate input (precipitation, flow and transport parameters) with output (piezometric head, velocity, flow rate, concertation, temperature, travel time….) considering heterogeneity of karst aquifers, but usually require extensive measurements and input data. These methods can be divided to equivalent porous medium (EPM), double porosity model (DPM), discrete conduit model (DCN) or Hybrid models (HM).

Hybrid models (HM), or coupled continuum pipe flow (CCPF) models, are the most complicated distributed models and they integrate discrete models and equivalent porous media models. HM were first developed by Király and Morel (1976), considering both conduit and matrix permeability in a karst system by using a finite difference method to simulate conduits and fractures as 1-D or 2-D elements located in a low permeability 3-D matrix. Further early applications include the work of Király (1985, 1988) and Király et al. (1995). Embedding discrete high conductivity features within a low permeability matrix continuum improves the pure continuum approach by introducing a spatially distributed high hydraulic conductivity network for the whole model area.

Careful above analysis of the state of the art of the karst flow modelling indicates that only hybrid distributed models, also known as hydrological integrated flow models, can potentially resolve complex karst Multiphysics, especially interrelation between matrix (if fracture permeability is resolved together with matrix one) and conduit exchange flow dynamics. Last two decades, some of the most important hybrid distributed flow models are developed as ModFlow-CFP (2005), Wash-123d (Yeh et al., 2006), HydroGeoSphere (Sudicky et al., 2013), ParFlow (Kollet and Maxwell, 2006) or Disco (deRooij, 2018), mainly based on finite elements or control volumes, i.e. 3-D elements for matrix flow (Darcy flow with Richards equation and

usally Van Genunchten unsaturated parameters) and 1-D elements for conduit flow (surface flow governed by St. Venant equations or approximate diffusive wave equation). Exchange between two flow domains are obtained using continuity of fluxes and pressures or via exchange flux parameter which is usually calibration prone. Our group developed CV_IGA karst flow model (Malenica et al., 2018) based on Control-Volume Iso-Geometric Analysis (Kamber et al., 2020, 2022; Gotovac et al., 2021) which is verified on unique 3-D laboratory physical models.

Transport karst models are also very sensitive, not only due to complex karst heterogeneities and related geometry, but also to strongly dependence on the quality of the karst flow model which is input to the transport analysis. Namely, small velocity errors can produce severe transport errors. Above hybrid models also usually has transport module which is based on advection-dispersion equation over both flow domains. Solute or energy exchange is usually enabled by advection or convection term without any new calibration parameters (i.e. Yeh et al., 2006 or Sudicky et al., 2013).

However, there are many limitations of distributed hydrological karst models to successful application in practice, especially at the scale of whole watershed. The main problem is requirement for so many parameters and measurements to completely describe complex karst processes. Despite progress of hydraulic and specially geophysics equipment's and measurement technologies, many information usually remains unresolved. The most missing information are usually matrix heterogeneity distribution (i.e. hydraulic conductivity, sorption, porosity), unsaturated (i.e. Van Genunchten) parameters and conduit network structure (depth, spatial location of conduits and/or its diameters and dimensions). Therefore, distributed hydrological karst models are difficult to verify, and our motivation was to build 3-D physical laboratory models in order to enable validation and verification of these models under strongly controlled laboratory conditions (Malenica et al., 2018, Malenica, 2019). In this paper, salt tracer tests have been performed under different flow and injection conditions including the different conduits with free and pressurized flow, with and without precipitation as well as borehole and surface

tracer injection. The main question remains whether complex distributed karst flow and transport model, based on Control Volume Isogeometric Analysis (CV-IGA), Eulerian-Langrage treatment of advection and dispersion and simple advection exchange term, can successfully reproduce salt tracer tests with good accuracy.

2. Experimental setup

Experimental setup presented in Figure 1 is described in detail in Malenica et al., 2018 and Malenica, 2019.

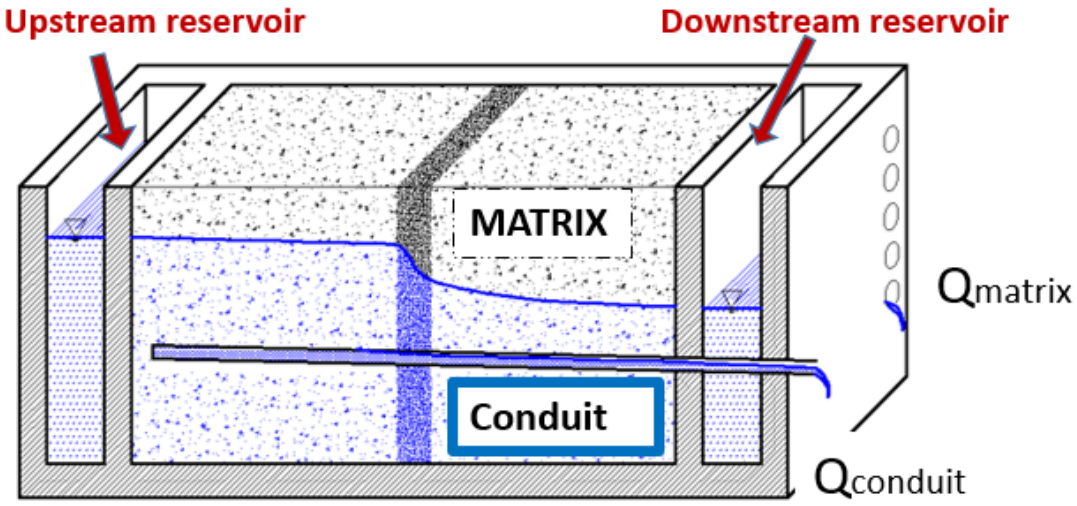

Figure 1. *Scheme of 3-D physical laboratory karst model.*

Length of the domain is 4 (m), width is 2.5 (m) and height is 2 (m). Flow in porous matrix is defined by hydraulic gradient between fixed water levels in upstream and downstream reservoirs using the specially designed wiers. 3-D model has three setups of conduits (perforated pipes): C1 – 12 mm inner diameter and perforated along the whole domain, C2 – 45 mm inner diameter and perforated along the upstream domain and C3 – 12 mm inner diameter as C1, but has perforated four branches (Figure 2). Vertical position of the conduits is 0.75 (m) from the bottom of physical model. Porous matrix is filled by coarse quartz sand (CQS), fine quartz sand (FQS) and gravel (G). Their proportion per layers of 25 cm is given in Table 1.

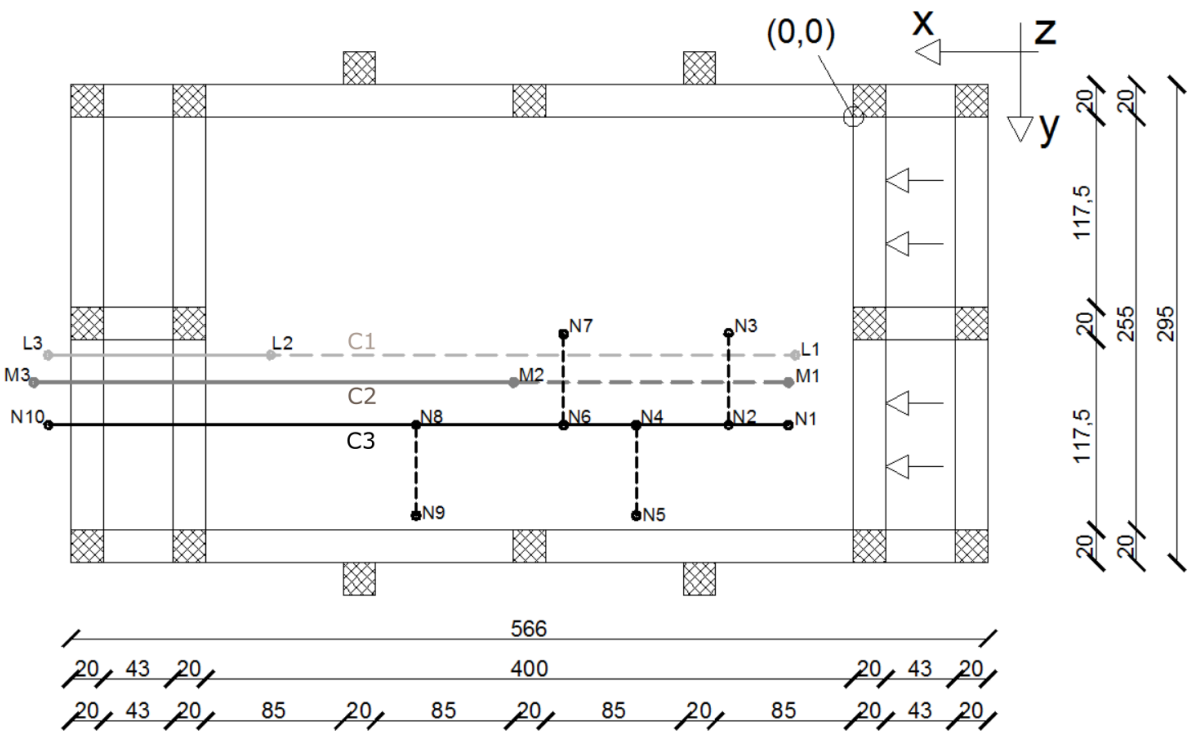

Figure 2. *Scheme of three setups of conduits: C1, C2 and C3.*

Table 2 yields saturated hydraulic properties of porous matrix. Unsaturated Van Gennunchten parameters can be found in Malenica et al., 2018.

Table 1. *Proportion of heterogeneous material inside the porous matrix per layers.*

	LAYER HEIGHT [cm]	LAYER THICKNESS [cm]	MATERIAL TYPE AND DISTRIBUTION		
			CQS [%]	FQS [%]	G [%]
Layer 1	0-25	25	11.69	0.81	-
Layer 2	25-50	25	10.76	0.81	0.93
Layer 3	50-75	25	7.54	4.34	0.62
Layer 4	75-100	25	6.89	4.34	1.27
Layer 5	100-125	25	9.48	0.92	2.10
Layer 6	125-150	25	10.89	0.81	0.80
Layer 7	150-175	25	10.10	1.94	0.46
Layer 8	175-200	25	-	-	12.5

Table 2. *Saturated hydraulic conductivity values of three porous materials.*

	Measurement range		Final value	
Material	K_{min} [m/s]	K_{max} [m/s]	K_H [m/s]	K_V [m/s]
CQS	$4.14 \cdot 10^{-4}$	$8.00 \cdot 10^{-3}$	$3.40 \cdot 10^{-3}$	$1.26 \cdot 10^{-3}$
FQS	$7.12 \cdot 10^{-5}$	$3.47 \cdot 10^{-4}$	$2.00 \cdot 10^{-4}$	$8.00 \cdot 10^{-5}$
G	$2.80 \cdot 10^{-2}$	$7.10 \cdot 10^{-2}$	$6.00 \cdot 10^{-2}$	$6.00 \cdot 10^{-2}$

Total flow rate in porous matrix is measured with help of weir in downstream reservoir. It is worthwhile to note that total porous matrix discharge in this way is not possible to measure in real catchment conditions. Both discharges, in porous matrix and conduits are measured by electromagnetic flowmeters. There are two sets of piezometers, lower 44 piezometers with pressure sensors and upper 20 piezometers with ECT sensors for measuring electrical conductivity and temperature. All piezometer and conduit geometry is given in Malenica et al., 2018. All mentioned signals are measured and recorded in the real time. Model is equiped with precipitation station, eight areas per 1.25 m2. Each area can generate separate precipitation distribution which means that station produces desired precipitation/rainfall in space and time.

In this paper, ten tracer tests are performed (Table 3). Tests 1-3 inject salt tracer in borehole B20. Tests 4-8 use surface injection on top of the model in area 1*1 m. Tests 9 and 10 use also surface injection, but uniform precipitation of 3 l/min with duration of 60 minutes. Table 3 presents time of injection and initial electrical conductivity. Some tests use only matrix flow, some of them smaller conduit C1 and another larger conduit C2. All these tracer tests enable analysis of different conduit setups, type of injection, initial concentration and influence of precipitation.

Table 3. *Setup of ten salt tracer tests.*

TRACER TEST		Test 1 M+C2	Test 2 M+ C1	Test 3 M	Test 4 M+ C2	Test 5 M+ C1	Test 6 M	Test 7 M	Test 8 M+ C2	Test 9 M+ C2	Test 10 M+ C1
FLOW (Steady state) m^3/h	Q_M	1.08	1.21	1.52	0.7	1.03	1.53	1.54	0.82	0.73	1.03
	Q_{C1}	-	0.67	-	-	0.83	-	-	-	-	0.88
	Q_{C2}	1.96	-	-	2.3	-	-	-	2.53	2.39	-
Tracer (Salt)	Injection	B24	B24	B24	1x1 m	1x1 m	1x1 m	1x1 m	1x1 m	1x1 m	1x1 m
	m (kg)	1	1	1	1	1	1	3	3	1	1
Rainfall simulation	Flow (l/min)	-			-			-		3	3
	Δt (min)									60	60

3. Mathematical model

Contaminant transport in karst aquifers is influenced by advection, dispersion, diffusion as well as degradation and other geochemical processes. (Delleur, 1999). In this work we describe basic processes such as advection and dispersion that are influenced by velocity (1-D for karst conduits and 3-D for porous matrix, Malenica, et al., 2018; Malenica, 2019) which presents the main input for the transport modelling. Flow solution is given by CV-IGA considering 1-D diffusive wave equation for conduits and 3-D Richards equation for porous matrix (Malenica et al., 2018). Conservative mass transport defined by advection and dispersion is described by well-known advection-dispersion equation for both flow domains (ADE; see for instance Zheng and Beneth, 2002 or de Rooij, 2013) with corresponding essential Dirichlet (D), natural Neumann (N) and mixed Cauchy boundary conditions:

$$\frac{\partial c}{\partial t} + \nabla(c \cdot \boldsymbol{v}) - \nabla(\boldsymbol{D_H} \cdot \nabla c) = cQ_p + c_R Q_R \quad (1)$$

$$c(\boldsymbol{x}) = c_D(\boldsymbol{x}) \rightarrow \boldsymbol{x} \in \Gamma_D \quad (1a)$$

$$\left(\boldsymbol{D_H} \cdot \nabla c(\boldsymbol{x})\right) \cdot \boldsymbol{n} = q_N(\boldsymbol{x}) \rightarrow \boldsymbol{x} \in \Gamma_N \quad (1b)$$

$$\left(c\boldsymbol{v} - \boldsymbol{D_H} \cdot \nabla c(\boldsymbol{x})\right) \cdot \boldsymbol{n} = q_C(\boldsymbol{x}) \rightarrow \boldsymbol{x} \in \Gamma_C \quad (1c)$$

where c is concentration $[{}^{M}/_{L^3}]$ of salt or contaminant, *v* is pore velocity in 3-D porous matrix or 1-D conduits, $Q_p[{}^{L^3}/_{L^3T}]$ is the sink term (negative sign), $Q_R[{}^{L^3}/_{L^3T}]$ is the source term (positive sign), and c_R $[{}^{M}/_{L^3}]$ is the concentration of the injected fluid. Boundary is the union of all segments with prescribe three type of boundary conditions 1a-1c ($\Gamma = \Gamma_D + \Gamma_N + \Gamma_C$). Dispersion tensor for porous matrix is defined as (Zheng and Beneth, 2002):

$$D_{Hij} = D^* \delta_{ij} + \alpha_T \, v \, \delta_{ij} + \left(\alpha_L - \alpha_T\right) \cdot \frac{v_i v_j}{v} \quad (2)$$

where δ_{ij} *is the* Kronecker delta symbol, *D** $[L^2/T]$ je molecular diffusion coefficient, while mechanical dispersion is reduced to finding two coefficients, longitudinal - α_L [L] and transversal dispersivity - α_T [L]. Mechanical dispersion obviously depends

on velocity defined in flow analysis. Dispersion in 1-D conduits is reduced to the diffusion coefficient (10^{-3} - 10^{-4} m^2/s).

Crux of the karst transport model lies in interaction between 1-D conduits and 3-D porous matrix (Yeh et al., 2006). Since both domains are described by ADE (1), mass exchange flux can be defined using only dominant advective flux. In that case exchange flux depends on orientation and magnitude of the exchange velocity between 3-D porous matrix (domain 1) and 1-D conduits (domain 2), $q_{ex}=\alpha_{ex}(h_c-h_m)$ where α_{ex} is exchange flow coefficient which needs to be calibrated in each particular case, h_c is the conduit head, and h_m is the piezometric head in porous matrix (see Figure 3; de Roij, 2013, Malenica et al., 2018):

$$F_{adv,ex} = q_{ex}c_*;\ c_* = c_1 = c_m \Longrightarrow q_{ex}\ \ oriented\ from\ matrix\ to\ the\ conduit$$
$$c_* = c_2 = c_C \Longrightarrow q_{ex}\ \ oriented\ from\ conduit\ \ to\ the\ matrix \quad (3)$$

Equation (3) relates to the definition of sink-source terms in ADE (1). Exchange velocity in (3) defined if that advective term is negative (sink) or positive (source) in both domains.

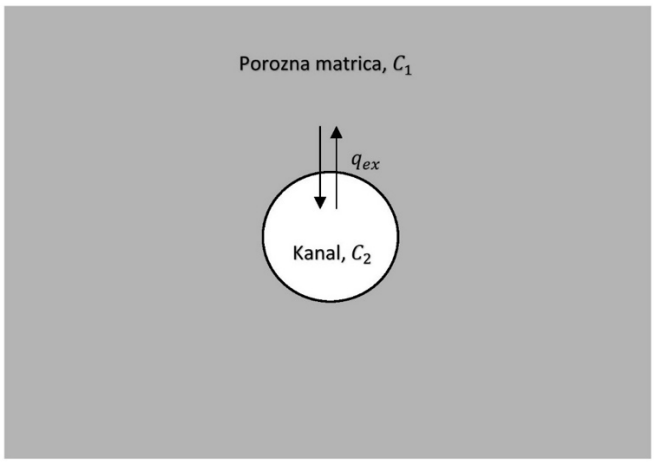

Figure 3. *Interaction between 1-D conduits and 3-D porous matrix.*

4. Numerical model

Numerical karst transport model will be created using mathematical model (1-3), weak formulation and isogeometric analysis (CV-IGA; Malenica et al., 2018, Malenica, 2019, Gotovac et al., 2021). ADE (1) needs to be multiplied by independent set of test functions:

$$\frac{\partial}{\partial t}\int_V cw dV + \int_V (\nabla(c\cdot\boldsymbol{v}) - \nabla(\boldsymbol{D_H}\cdot\nabla c))w dV + \int_V \left(cQ_p\right) w\, dV = \int_V \left(q_{ex}c_* + c_R Q_R\right) w\, dV \quad (4)$$

Domain is divided to the smaller control volumes - V_i that are defined by unit test functions:

$$w_i(\boldsymbol{x}) = 1 \rightarrow \boldsymbol{x} \in V_i \;\; or \; w_i(\boldsymbol{x}) = 0 \rightarrow \boldsymbol{x} \notin V_i \quad (5)$$

Using the weak formulation and Green-Gauss-Ostrogradski theorem, volume integrals in (4) becomes surface integrals per control volume boundaries ∂V_i:

$$\frac{\partial}{\partial t}\int_{V_i} cdV_i + \int_{\partial V_i}((c\cdot v) - (D_H\cdot\nabla c))\boldsymbol{n}d\partial V_i + \int_{\Gamma_i}((c\cdot v) - (D_H\cdot\nabla c))\boldsymbol{n}d\Gamma_i + (cQ_P)_i = \int_{V_{ex\_i}}(q_{ex}c_*)\, dV_{ex\_i} + (c_R Q_R)_i \quad (6)$$

where ∂V_i is inner surface area of i-th control volume, Γ_i is the boundary surface area of i-th control volume, while $\boldsymbol{n}$ is outward normal and V_{ex_i} is the surface exchange area between conduits and porous matrix according to the Equation (3). Formally, second and third terms are the same, but operate on different surface areas. Especially, third term is important due to satisfying boundary conditions (1a-1c). Not that union of all non-overlapped control volumes covers the whole domain volume - *V*.

There are many numerical techniques for solving weak form of ADE(6): (a) Eulerian methods such as finite elements or control volumes; (b) Langrangian methods such as Random Walk Particle Tracking (RWPT) and (c) hybrid (Euler-Langrange) methods [i.e. Zheng and Bennet, 2002].

ADE (6) usually becomes advection dominated and numerically unstable for Eulerian methods. Peclet grid number $Pe_i = \frac{v_i \Delta x_i}{D_{ii}} \leq 2\,;\; i = x, y, z$ requires very fine grid size. Furthermore, Courant number requires small time step sizes due to small spatial grid and these methods become intractable. On the other side, RWPT

methods also present instabilities in presence of high heterogeneity and singularities, as in karst flow and transport models.

Therefore, we use in this paper third option, hybrid Eulerian-Langrange methodology [Zheng i Bennet, 2002], such that advection is solved by Langrangian backward particle tracking method, while dispersion, exchange terms and boundary conditions are solved by Eulerian CV-IGA, analogues as in the karst flow model (Malenica et al., 2018).

In the first Langrangian backward particle step, advection is solved using concentration calculation in Gauss points $x_k(t_{n+1})$ of control volumes such that we calculate position of that point in the beginning of time step $x_k(t)$ using the particle trajectory motion:

$$\boldsymbol{x}_k(t_n) = \boldsymbol{x}_k(t_{n+1}) + \int_{t_{n+1}}^{t_n} \boldsymbol{v}\,[\boldsymbol{x}_k(\xi)]d\xi \tag{7}$$

Advection time step is bounded by Courant-Freidrich-Levy (CFL) criterion $\frac{v_i \Delta t}{\Delta x_i} \leq \frac{1}{2}$. Advection step Δt should be small enough that do not cross half control volume in any direction. Along advection trajectory, concentration in each Gauss point is the same along the whole time step:

$$(c(\boldsymbol{x}_k(t_n)) = c(\boldsymbol{x}_k(t_{n+1}))) \tag{8}$$

Concentration in each domain (m – porous matrix, c – conduit) is described by linear combination of independent Fup basis functions and related unknown coefficients (the same grid as in CV-IGA flow solution) which need to be solved in each (n+1)-th time step:

$$c_*(\boldsymbol{x}, t_{n+1}) = \alpha_{*j}^{n+1}(\boldsymbol{x})\varphi_{*j}(\boldsymbol{x}); \qquad _* = m, c \tag{9}$$

Number of basis functions is equal to the number of control volumes in each flow domain. Advective step is calculated from (8) using (9):

$$\alpha_{*j}^{n+1,A} \int_{V_i} \varphi_{*j}(\boldsymbol{x})\, dV_i = \int_{V_i} c_*^A(\boldsymbol{x}, t_{n+1})\, dV_i\,; \qquad _* = m, c \tag{10}$$

Indexes of test functions denote raw and indexes of basis functions denote column of mass consistent matrix $M_{ij}^C = \int_{V_i} \varphi_{*j}(\boldsymbol{x})\, dV_i$. Both integrals in (10) should be solved by Gauss numerical integration (Malenica, 2019). Integral function on right

side is obtained using (7) and (8) as well as explained „particle backward Lagrangian“ algorithm for each Gauss integration point. Here, we use explicit Runge-Kutta-Verner 6(8) time integration in (7), see Gotovac et al., 2009.

Obtained advective concentration field (9) becomes initial condition for the second dispersive step in the current total time step. In the second dispersive step, advection is removed, and basically we use similar CV-IGA concept and the same grid as for flow solution because essentially dispersive type of process is considered. ADE (6) then change the form in the following way:

$$\frac{\alpha_{*j}^{n+1}-\alpha_{*j}^{n+1,A}}{\Delta t}\int_{V_i}\varphi_{*j}(\boldsymbol{x})\,dV_i+\alpha_{*j}^{n+1}\int_{\partial V_i}\left(-\boldsymbol{D}_{*\boldsymbol{H}}\cdot\nabla\varphi_{*j}(\boldsymbol{x})\right)\cdot\boldsymbol{n}d\partial V_i+\alpha_{*j}^{n+1}\int_{\Gamma_{*Di}}\left(-\boldsymbol{D}_{*\boldsymbol{H}}\cdot\nabla\varphi_{*j}(\boldsymbol{x})\right)\cdot\boldsymbol{n}d\Gamma_{*Di}+\alpha_{*j}^{n+1}\int_{\partial\Gamma_{*Di}}\varphi_{*j}(\boldsymbol{x})d\Gamma_{*Di}-\alpha_{*j}^{n+1}\int_{V_{*ex_i}}\left(q_{ex}\varphi_{*j}(\boldsymbol{x})\right)dV_{*ex_i}-$$

$$Q_P\varphi_{*j}(\boldsymbol{x_i})=\int_{\Gamma_{*Ni}}q_{*N}d\Gamma_{*Ni}+\int_{\Gamma_{*Di}}c_{*D}(\boldsymbol{x})d\Gamma_{*Di}+\int_{V_{ex\_i}}(q_{ex}c_*)\,dV_{ex\_i}+(c_RQ_R)_i$$

; $_* = m, c$ (11)

For both flow domains, the first term at the left side presents unsteady time term described by backward Euler time integration scheme using unknown Fup coefficients and known „initial“ Fup coefficients from the advective step. Since all other spatial terms depend on unknown dispersive Fup coefficients, it presents implicit Eulerian time integration scheme. Second left term presents dispersive term over inner surface areas of control volumes. Fifth left term and third right term presents advective exchange mass flux (3) between 1-D conduits and 3-D porous matrix. Depending of direction of flux exchange q_{ex} from (3) and Figure 3, this term in one domain lies on the left side, and in another domain is on the right side as source term. In the flow domain where exchange concentration in (3) is equal to the concentration from another domain, this term becomes source term and vice versa. In that case q_{ex} in (3) is positive because that term represents source term. The first right term describes satisfaction of Neumann (N) boundary conditions (1b) in the classical weak form as known dispersive flux on that part of boundary (as in CV-IGA for flow solution, see Malenica, 2019). The third left term presents dispersive flux on Dirichlet boundary that has the same form as the second left term. The

second right and fourth left terms have the form $\int_{\Gamma_{*Di}}(c - c_{*D}(\boldsymbol{x}))d\Gamma_{*Di}$ and present implementation of essential Dirichlet (D) boundary conditions (1a) in the weak form. This term can be regard as penalization term where calibration parameter is one (used in CV-IGA for flow solution in Malenica et al., 2018) or non-parametric Nitsche weak form (i.e. Fernandez-Mendez and Huerta, 2004; Kollmannsberger et al., 2015). Non-parametric Nitsche weak form has the additional term $\int_{\Gamma_{*Di}}(c - c_{*D}(\boldsymbol{x}))\nabla w \cdot \boldsymbol{n} d\Gamma_{*Di}$, but it is equal to zero in CV-IGA due to properties of test functions in (5) on Dirichlet (D) boundary. The last terms on both sides present sink and source terms, respectively.

Note that linear systems (10-11) are valid for both flow domains. However, calculation is consistent if 1-D conduits include corresponding cross section area at each control volume. Here we use constant circle area within each control volume, but diameter can differ between control volumes which is not significant limitation. Linear systems (10-11) are solved by IMSL routine Pardiso (see Malenica, 2019). Firstly, advective systems (10) are solved for both domains, then dispersive step (11) is solved sequentially in both domains using iterative calculation until the desired accuracy.

5. Results

Ten tracer tests are performed, and input data are given in Table 3. We will choose three characteristic tracer tests 2, 4 and 9 to show different properties of tracer tests as well as verification with developed CV-IGA transport model.

Tracer test 2 is presented in Figure 4. Borehole tracer injection is performed in B24, conduit C1 with pressurized flow is open and there is no precipitation. Selected ECT sensors show very quick response of concentration signal. Duration of injection was 45 minutes. After approximately ten hours 99% of salt disappears from the domain. Every ECT sensor shows approximately log-normal shape of the breakthrough curve. Downstream sensors exhibit lower peak, but larger time response, as it is expected from the dispersion process. Initial injected fluid

concentration is 9300 (μS/cm). Conduit C1 has peak concentration around 10% of initial concentration that is very high if matrix and conduit flow is compared.

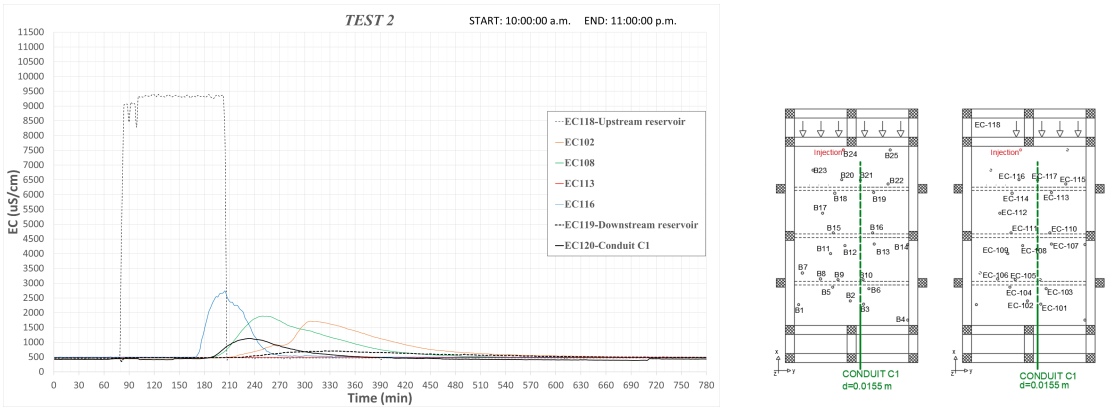

Figure 4. *Tracer test 2: Borehole injection in B24, matrix + conduit C1 and no precipitation.*

Figure 5 presents comparison between measured and simulated breakthrough curves in four selected ECT sensors. Comparison is generally satisfactory, especially for conduit C1. All peaks have similar arrival times, also time duration of concentration response is very close.

Tracer test 4 is presented in Figure 6. Borehole tracer injection is performed surface injection, conduit C2 with free surface flow is open and there is no precipitation. Selected ECT sensors show very quick response of concentration signal. Duration of injection was 15 minutes. After approximately ten hours 99% of salt disappears from the domain, as in test 2. Every ECT sensor shows approximately log-normal shape of the breakthrough curve. Initial injected fluid concentration is 11500 (μS/cm). Conduit C2 has lower peak concentration than C1 in test 2. ECT 119 is installed in downstream reservoir. Its concentration has no direct physical meaning because it is mixed discharge water but contains information about total duration of tracer test.

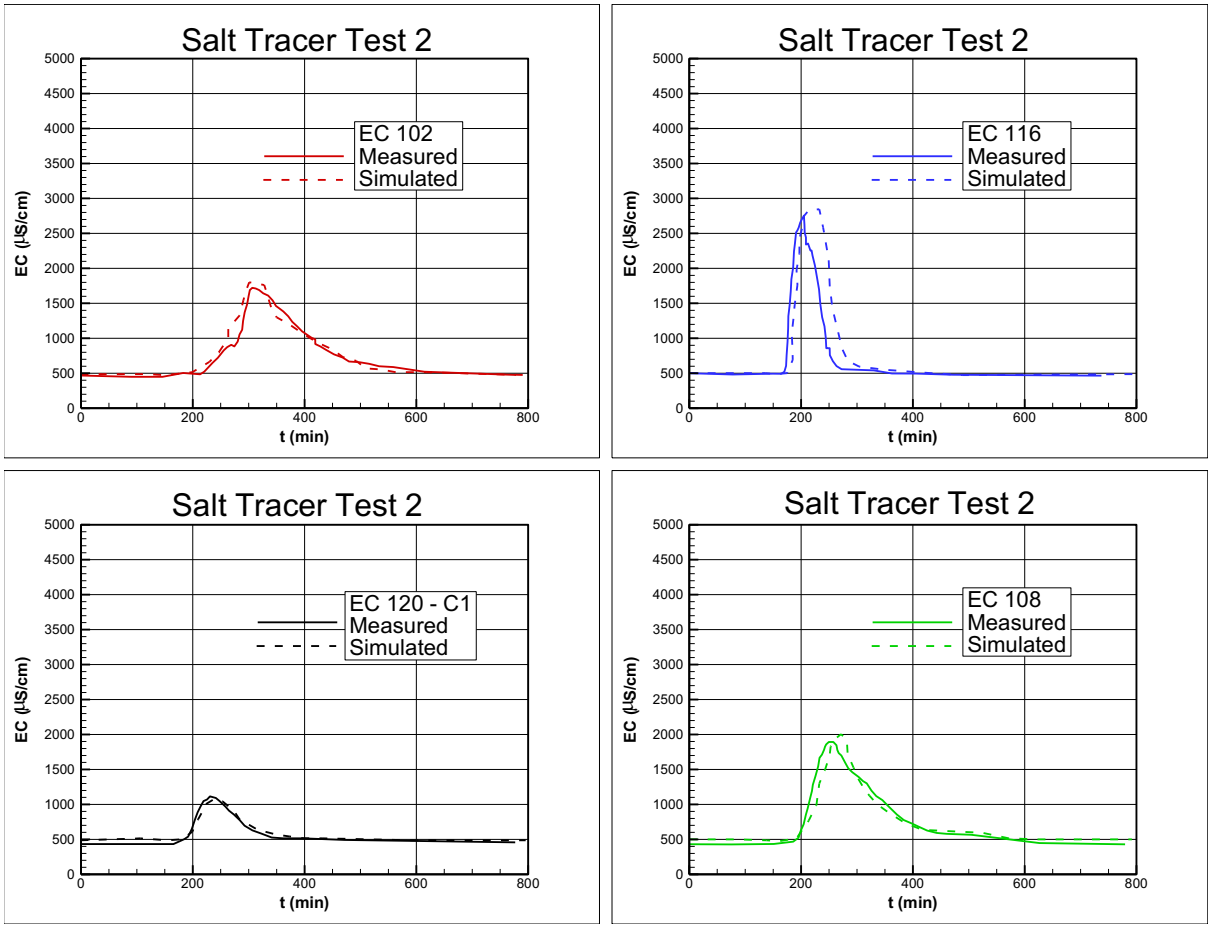

Figure 5. *Tracer test 2: Comparison between measured and simulated breakthrough curves in four selected ECT sensors.*

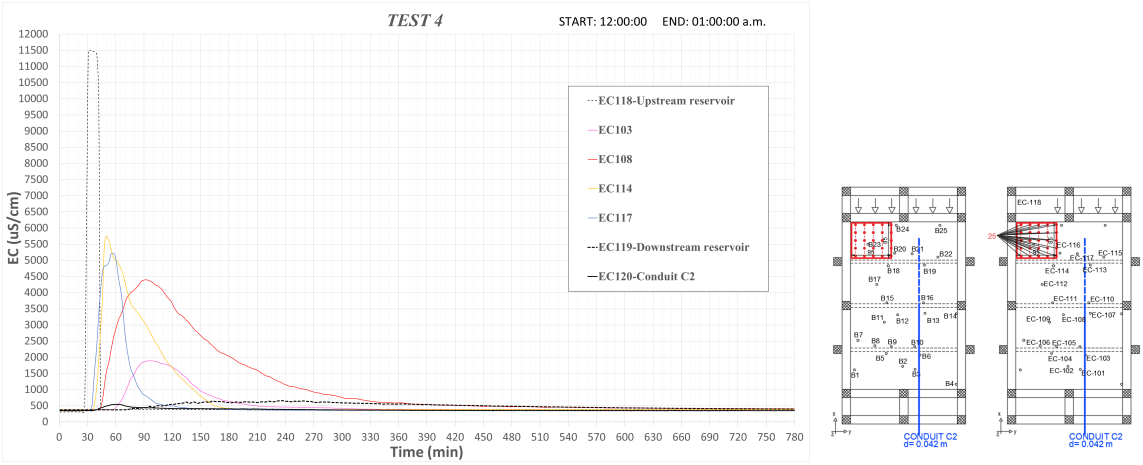

Figure 6. *Tracer test 4: Surface injection, matrix + conduit C2 and no precipitation.*

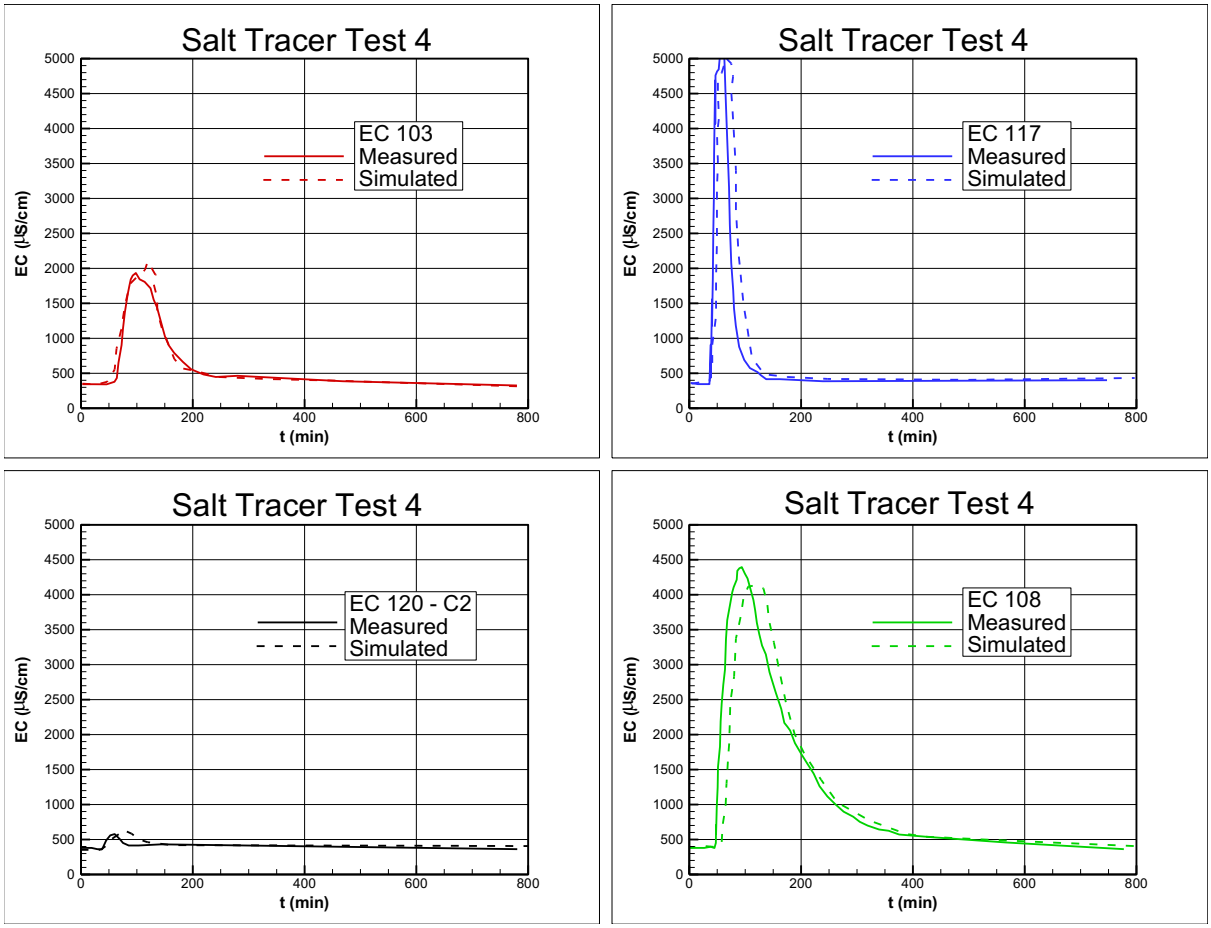

Figure 7. *Tracer test 4: Comparison between measured and simulated breakthrough curves in four selected ECT sensors.*

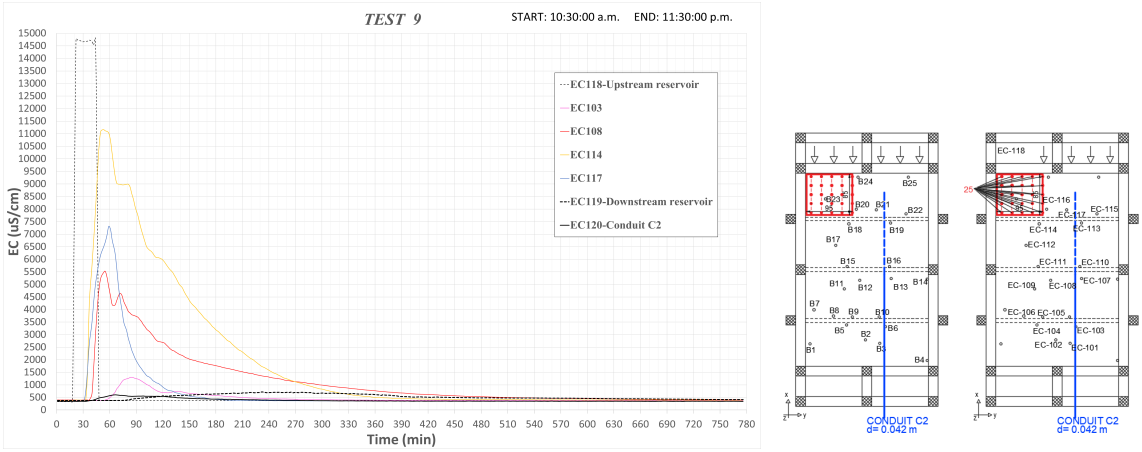

Figure 8. *Tracer test 9: Surface injection, matrix + conduit C2 and with precipitation.*

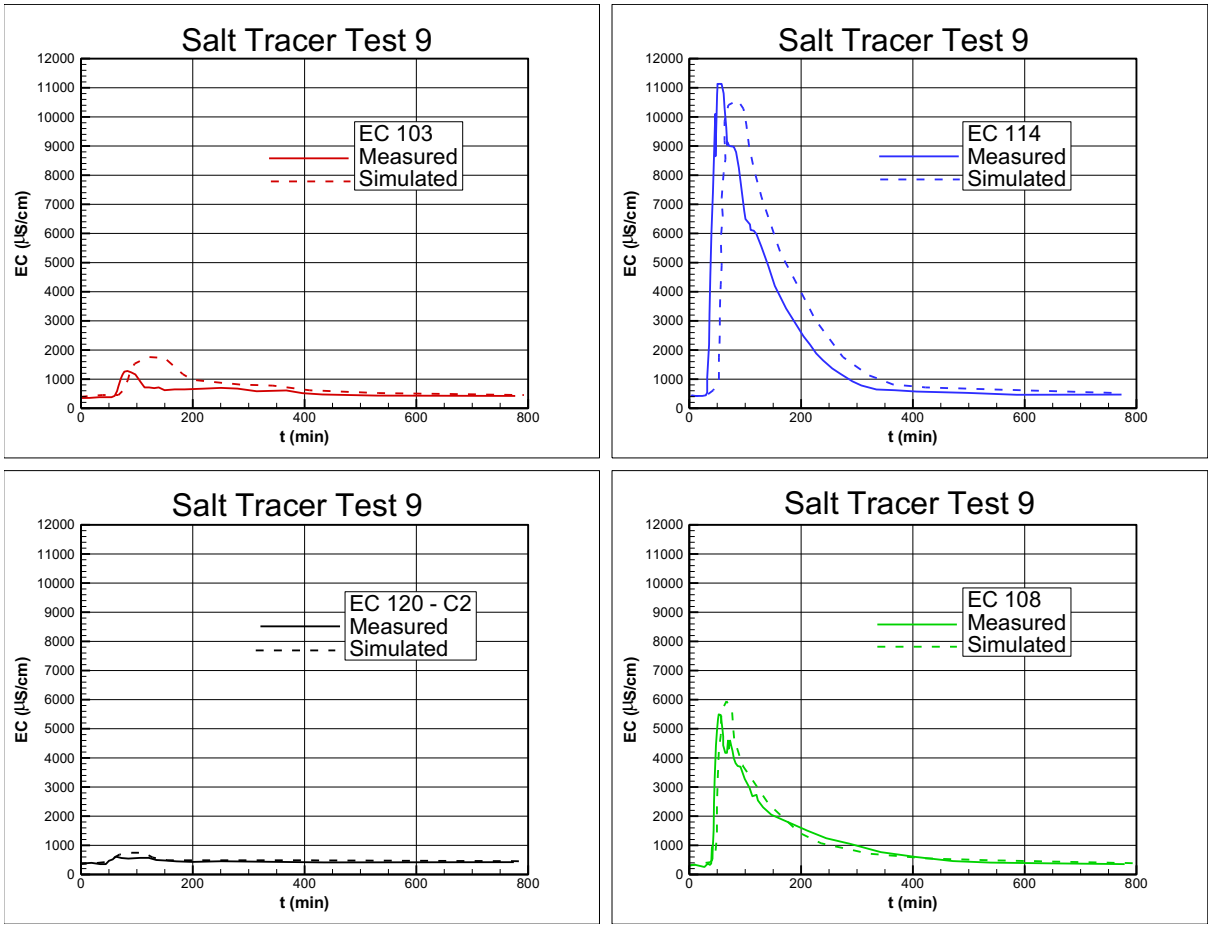

Figure 9. *Tracer test 9: Comparison between measured and simulated breakthrough curves in four selected ECT sensors.*

Tracer test 9 is presented in Figure 8. Borehole tracer injection is performed as surface injection, conduit C2 with free surface flow is open and there is uniform precipitation of 3 l/min with total duration of 60 minutes (Table 3). This Tracer Test differs from Test 4, mainly due to influence of precipitation. Selected ECT sensors show again very quick response of concentration signal. Duration of injection was 15 minutes. Initial injected fluid concentration is 14700 (µS/cm). Conduit C2 has again lower peak concentration than C1 in test 2. Breakthrough curves now show bimodal response. Reason for that lies in additional precipitation effect that pushes salt plume to the exit of the domain.

Figures 7 and 9 show comparison between measured and simulated breakthrough curves in four selected ECT sensors. Comparison is generally satisfactory. All peaks have similar arrival times, also time duration of concentration

response is very close. Presented results confirm that developed CV-IGA transport karst model can describe complete behavior of salt migration from injection location to the domain exit in porous matrix. Moreover, conduit concentration is also accurately capturing that confirms that model correctly describe exchange salt flux between 1-D conduits and 3-D porous matrix.

6. Conclusions

This study reveals experimental unique setup for karst flow and transport modeling. Large 3-D physical model is built in order to verify and validate reliable karst flow and transport model. Ten tracer tests are performed under different flow and injection conditions including the different conduits with free and pressurized flow, with and without precipitation as well as borehole and surface tracer injection. Results show that complex distributed karst flow and transport model is needed, based on Control Volume Isogeometric Analysis (CV-IGA), Eulerian-Langrage treatment of advection and dispersion and simple advection exchange term, to successfully reproduce salt tracer tests with good accuracy.

Acknowledgments

This research was funded by the Croatian Science Foundation (in Croatian: Hrvatska zaklada za znanost -HRZZ) through the scientific project “Multiphysics modelling of surface-subsurface water systems”, grant number: IP-2020-02-2298.
This research is partially supported through project KK.01.1.1.02.0027, a project co-financed by the Croatian Government and the European Union through the European Regional Development Fund - the Competitiveness and Cohesion Operational Program.

7. References

M. Bakalowicz, “Karst groundwater: A challenge for new resources”, Hydrogeology Journal, vol. 13, no. 1, pp. 148–160, 2005.

Teutsch G., Sauter M., Groundwater modeling in karst terranes: Scale effects, data acquisition and field validation. — Third Conference on Hydrogeology, Ecology,

Monitoring, and Management of Ground Water in Karst Terranes. National Ground Water Association, Dublin, Ohio: 17-35, 1991.

M.S. Field, S.G. Nash. Risk assessment methodology for karst aquifers:(1) Estimating karst conduit-flow parameters. Environmental Monitoring and Assessment, 47, 1–21, 1997. L. Király. Karstification and groundwater flow. Speleogenesis and Evolution of Karst Aquifers, 1:155–192, 2003.

Kovacs A., Sauter M., Modelling karst hydrodynamics. In: D. Goldscheider N & Drew, ed. Methods in Karst Hydrogeology, Taylor & Francis, London: 201-222, 2007.

M. Sauter, T. Geyer, A. Kovács, G. Teutsch. Modellierung der hydraulik von karstgrundwasserleitern–eine übersicht. Grundwasser, 11:143–156, 2006.

L. Király, G. Morel. Etude de r´egularisation de l'Areuse par mod`ele math´ematique. Bulletin d'Hydrog´eologie de l'Universit´e de Neuchˆatel, 1: 19-36, 1976.

A.W. Harbaugh, MODFLOW-2005, The U.S. Geological Survey Modular GroundWater Model-the Ground-Water Flow Process, 2005.

Yeh, G. T., et al., "A first principle, physics-based watershed model: WASH123D." Watershed models, V. P. Singh, and D. K. Frevert, eds., CRC, Boca Raton, Fla. 2006.

Kollet, S.J.; Maxwell, R.M., Integrated surface–groundwater flow modeling: A free-surface overland flow boundary condition in a parallel groundwater flow model. Adv. Water Resource, 29, 945–958, 2006.

Malenica L, Gotovac H, Kamber G, Simunovic S, Allu S, Divic V. Groundwater flow modeling in karst aquifers: Coupling 3-D matrix and 1-D conduit flow via control volume isogeometric analysis-Experimental verification with a 3-D physical model. Water. Dec 5; 10(12):1787, 2018.

G. Kamber, H. Gotovac, V. Kozulić, L. Malenica, B. Gotovac: Adaptive numerical modeling using the hierarchical Fup basis functions and control volume isogeometric analysis, International Journal for Numerical Methods in Fluids, 92(10), 1437-1461, 2020.

G. Kamber, H. Gotovac, V. Kozulić, and B. Gotovac, "2-D local hp adaptive isogeometric analysis based on hierarchical Fup basis functions," Computer Methods in Applied Mechanics and Engineering, vol. 398, p. 115272, 2022.

Gotovac, Hrvoje; Malenica, Luka; Gotovac, Blaž. Control Volume Isogeometric Analysis for groundwater flow modeling in heterogeneous porous media. // Advances in water resources, 148:103838, 2021.

Luka Malenica, Numerical modeling based on spline basis functions: Application to groundwater flow modeling in karst aquifers and advection dominated problems (In Croatian). PhD thesis.